

**Improved hydrothermal stability of Pd nanoparticles on nitrogen-doped carbon supports**

Journal:	<i>Catalysis Science &amp; Technology</i>
Manuscript ID	CY-ART-05-2018-000947.R1
Article Type:	Paper
Date Submitted by the Author:	08-Jun-2018
Complete List of Authors:	Huo, Jiajie; Iowa State University, Chemical and Biological Engineering Department; Iowa State University Duan, Pu; Brandeis University, Chemistry Department Pham, Hien; U. New Mexico, Chemical & Biological Engineering Chan, Yee Jher; Iowa State University, Chemical & Biological Engineering Datye, Abhaya; University of New Mexico, Department of Chemical and Nuclear Engineering Schmidt-Rohr, Klaus; Brandeis University, Chemistry Shanks, Brent; Iowa State University, College of Engineering



## Catalysis Science &amp; Technology

## ARTICLE

## Improved hydrothermal stability of Pd nanoparticles on nitrogen-doped carbon supports

Received 00th January 20xx,  
Accepted 00th January 20xx

DOI: 10.1039/x0xx00000x

www.rsc.org/

Jiajie Huo,<sup>ab</sup> Pu Duan,<sup>bc</sup> Hien N. Pham,<sup>bd</sup> Yee Jher Chan,<sup>a</sup> Abhaya K. Datye,<sup>bd</sup> Klaus Schmidt-Rohr<sup>bc</sup> and Brent H. Shanks<sup>ab\*</sup>

Carbon supports have been shown to provide better hydrothermal stability than alumina or silica supports, thus attracting more attention for aqueous-phase biomass conversion reactions. However, sintering and leaching of the metal particles still occur during condensed phase utilization of carbon supported metal catalysts. To further improve the stability of supported metal particles, a simple nitrogen-doped carbon coated SBA-15 was synthesized and systematically characterized. Better stability of supported Pd particles was found from nitrogen incorporation into the carbon support during extended hydrothermal treatment or continuous flow reaction conditions. With these materials, leaching was negligible and sintering was suppressed. Based on solid-state <sup>15</sup>N and <sup>13</sup>C NMR analysis before and after hydrothermal treatment, the improved dispersion and stability from nitrogen doping was ascribed to pyridine, pyrrole, and imidazolium groups. Relatively small carbon fragments resulting from nitrogen incorporation rendered more silica exposure to water and concomitant hydrolysis, but the stability and activity of Pd particles was preserved. The Pd stability advantage was also observed on nitrogen-doped carbon coatings of silica gel and CMK-3 supports. The enhanced stability of Pd particles on different nitrogen-doped carbon materials was correlated with the synergistic effect of oxygen and nitrogen heteroatoms and formation of a decorative carbon overlayer on the Pd particles.

## Introduction

Biomass conversion continues to attract significant attention as a potentially more sustainable approach to produce value-added fuels and chemicals.<sup>1-5</sup> These conversions commonly are performed in the aqueous phase at various temperatures, but the short term screening studies often used neglect to account for limited hydrothermal stability of many heterogeneous catalysts. Therefore, stability under realistic reaction conditions remains a challenge.<sup>6-9</sup> Previous efforts have focused on carbon coating of metal oxides, such as alumina and silica, which was shown to increase hydrothermal stability.<sup>10, 11</sup> We have also demonstrated that low-temperature-synthesized carbon with more oxygen functional

groups can help disperse and stabilize Pd nanoparticles compared with high temperature carbon supported Pd catalyst.<sup>12</sup> However, the carbon coated oxide supported metal catalysts still suffer deactivation after repeated hydrothermal treatments due to leaching and sintering of the metal phase.<sup>12</sup> Carbon as an overcoat on supported Pd catalysts has also been shown to improve stability,<sup>13</sup> but the thin carbon layers can cover and block some of the active sites as well. Silica has been reported to improve the hydrothermal stability of niobia, ZrO<sub>2</sub> and TiO<sub>2</sub>, but was still not stable over the long term.<sup>14, 15</sup> Among various metal oxides, TiO<sub>2</sub> was found to be stable only with very low surface areas (< 52 m<sup>2</sup>/g).<sup>15</sup> Nitrogen-doped carbon materials have been explored extensively for electrochemical catalysis,<sup>16-20</sup> supercapacitors,<sup>21</sup> oxidation catalysts,<sup>22</sup> catalyst supports,<sup>23-28</sup> and adsorption.<sup>29-31</sup> Improved activity and selectivity have been specifically observed with nitrogen-doped carbon supported Pd catalysts.<sup>24-26</sup> However, these research were mainly conducted in batch reactor with water or organic solvents at low temperature (less or equal to 100°C) for a short period of time (less than 3 hours), which are insufficient to study stability relative to real reactor operation utilizing flow conditions at higher temperature. Moreover, stability studies typically involved repeated batch reactions with complete conversion were performed, which could benefit from excess catalyst loading, so limited detailed information on the catalyst stability is available.<sup>24, 25</sup>

<sup>a</sup> Department of Chemical and Biological Engineering, Ames, Iowa 50011, United States

<sup>b</sup> Center for Biorenewable Chemicals, Iowa State University, Ames, Iowa 50011, United States

<sup>c</sup> Department of Chemistry, Brandeis University, Waltham, Massachusetts 02453, United States

<sup>d</sup> Department of Chemical and Biological Engineering and Center for Microengineered Materials, University of New Mexico, Albuquerque, New Mexico 87131, United States

<sup>e</sup> Ames Laboratory, U.S. Department of Energy, and Department of Chemistry, Iowa State University, Ames, Iowa 50011, United States

† Electronic Supplementary Information (ESI) available. See DOI: 10.1039/x0xx00000x

Graphite nitrides have been studied extensively and found to yield improved stability and activity, but usually the surface area is very low ( $< 10 \text{ m}^2/\text{g}$ ).<sup>32, 33</sup> To overcome this shortcoming, mesoporous graphite nitrides have been explored by using a template, usually with the help of HF etching after nanocasting on mesoporous silicas such as SBA-15.<sup>26, 34</sup> However, this process poses significant chemical handling challenges.

While nitrogen-doped carbon materials showed better activity and stability, the chemical interactions leading to improved activity and stability are still unclear. XPS has been the main technique used to quantify different nitrogen functional group in these materials.<sup>22, 24-26, 28, 35</sup> Unfortunately, the accuracy of XPS interpretation depends on the peak deconvolution procedure used and the resolution of the instrument.<sup>36</sup> Ideally, a complementary technique could be developed that helps refine understanding of the chemical nature of the nitrogen-doped carbon. Therefore, an important contribution of the current study was to use solid-state NMR to quantitatively evaluate the nitrogen- and oxygen-containing functional groups in the carbon matrix.

As carbon coating have successfully improved the hydrothermal stability of silica and Pd particles, we further introduced nitrogen into the carbon coating in order to further stabilize Pd particles. Coating nitrogen-doped carbon on SBA-15 also allowed us to use  $^{13}\text{C}$  and  $^{15}\text{N}$  solid-state NMR to investigate the chemical moieties on the catalyst surface. A simple nitrogen-doped carbon coated SBA-15 supported Pd catalysts was prepared, which show improved stability of Pd particles under hydrothermal conditions for extended time. While the silica structure collapsed as a result of smaller carbon fragments in the carbon coating after nitrogen incorporation, the same stabilization of Pd particles was observed on CMK-3, which maintained its structure during hydrothermal treatment. The nitrogen doping effect on Pd particles was characterized by the traditional XPS, BET surface area, high angle annular dark field (HAADF)-STEM, and high resolution TEM (HRTEM) approaches as well as advanced  $^{13}\text{C}$  and  $^{15}\text{N}$  solid-state NMR before and after hydrothermal reactions.

## Experimental

### Catalyst preparation

The nitrogen-doped carbon materials were synthesized using the following procedure. First, SBA-15 was synthesized according to the literature.<sup>37</sup> Melamine (0.1 g, 99%, Sigma-Aldrich) and glucose (0.5 g, D-glucose anhydrous, Fisher Scientific) were dissolved in nanopure water and then SBA-15 (1 g) was added into the mixture. The resulting aqueous solution with SBA-15 was stirred in an open evaporating dish at room temperature overnight until the water was evaporated and white solid was obtained. The white solid was ground, transferred into a quartz boat, and pyrolyzed in a quartz tube in a tube furnace under UHP argon flow at 300 °C, 400 °C or 600 °C for 10 h with a ramp rate of 5 °C/min. The

nitrogen-doped carbon coated SBA-15 was denoted as 300, 400 or 600NC/SBA-15 depending on the pyrolysis temperature. After washing with hydrochloric acid (1 M), the NC/SBA-15 was then washed with deionized water and vacuum filtered. As a reference, carbon coated SBA-15 was synthesized in a similar manner without melamine and denoted C/SBA-15.  $^{13}\text{C}$ -labeled D-glucose,  $^{15}\text{N}$ -labeled melamine, and  $^{13}\text{C}$ -labeled melamine were reacted in the same manner for use in the  $^{13}\text{C}$  and  $^{15}\text{N}$  NMR studies. To examine the effect of the support, nitrogen-doped carbon coating was also synthesized at 300 °C using the same method on an amorphous silica gel (high-purity grade DAVISIL Grade 636, Sigma Aldrich) and on an ordered mesoporous CMK-3 carbon material. These were denoted as 300NC/silica gel and 300NC/CMK-3, respectively. The CMK-3 was synthesized according to the literature.<sup>38</sup> In addition, 300NC/SBA-15s with different amounts of melamine were also synthesized while keeping the glucose and SBA-15 amounts the same. Incipient wetness impregnation was used for introducing the 5 wt% Pd on the carbon-coated materials using palladium acetate (99.98%, Sigma Aldrich) dissolved in acetone. The catalysts were dried at room temperature and reduced in a tube furnace at 200 °C under 200 mL/min hydrogen gas flow for 2 h with a ramp rate of 2 °C/min.

### Catalyst characterization

An ASAP 2020 (Micromeritics) was used to perform BET surface area analysis at -196 °C with liquid nitrogen. Nitrogen physisorption was performed after degassing at 150 °C for 10 hr. Pore volume was reported at a relative pressure of 0.97. Pore size distribution from adsorption isotherm was calculated by the BJH method. CO pulse chemisorption was measured on an ASAP 2920 (Micromeritics) coupled with a TCD detector. Hydrogen reduction at 200 °C for 2 h was followed by flushing with UHP argon for 15 min before analysis. A stoichiometric factor of 2 was used for the dispersion calculations.<sup>39, 40</sup> A Kratos Amicus/ESCA 3400 was used to perform X-ray photoelectron spectroscopy (XPS) analysis. Unmonochromated Mg K $\alpha$  X-ray radiation was used as the X-ray source with CasaXPS software used to process the raw data. A CHNS elemental analyzer (Vario MICRO cube) was used to perform elemental analysis. ICP-OES was performed on a PerkinElmer Optima 8000 ICP-OES Spectrometer with Pd loading quantified after the catalyst was digested in freshly-made aqua regia for 24 hr. For electron microscopy, the samples were dispersed in ethanol and mounted on holey carbon grids for examination in a JEOL 2010F 200 kV transmission electron microscope (resolution of 0.14 nm). Images were recorded in high angle annular dark field (HAADF) and bright-field (HRTEM) modes. At least 250 particles were counted for each catalyst in the particle size distribution analysis.

### Hydrothermal treatment

Hydrothermal treatment was performed in the aqueous phase at 170 °C for 48 h following the same method described

previously.<sup>12</sup> A known amount of catalyst was loaded in a 10 mL thick-wall glass vial together with 6 mL of nanopure water. After capping tightly, the glass vials were placed in an oil bath at 170 °C with 400 rpm stirring for 48 h. The catalysts were filtered and washed with DI water, while the aqueous filtered solution was analyzed by ICP-OES to determine the amount of leached Pd.

### Reaction testing

Liquid phase furfural hydrogenation was performed on the catalyst in a fixed-bed reactor as described elsewhere.<sup>41</sup> Before reaction, the catalyst (20 mg) was reduced in-situ in the reactor with 200 mL/min H<sub>2</sub> (UHP, Airgas) at 200 °C for 30 min (heating tape, a type K thermocouple and a Omega CS132K PID controller). The reaction was performed at 130 °C. The H<sub>2</sub> gas flow rate of 20 mL/min was controlled by a mass flow controller (Brooks SLA5850). The furfural solution (10 g/L) was fed into the reactor by a high performance liquid chromatograph (HPLC) pump (Series I) at a rate of 0.04 mL/min. All reactions were performed at the same conditions. A back-pressure regulator was used to maintain the H<sub>2</sub> pressure at 750 psi. The liquid solution was accumulated in a condenser at the top of the reactor, sampled periodically, and filtered with a 0.2- $\mu$ m syringe filter for gas chromatograph analysis (Agilent 7890A with a flame ionization detector (FID) and a HP-5ms column). The carbon balances for reactions were calculated based on furfural, furfuryl alcohol, and tetrahydrofurfuryl alcohol and were usually above 90% except those for Pd 600C/SBA-15 and Pd 300NC/SBA-15 (20:8), which were above 85%.

### Solid-state <sup>15</sup>N and <sup>13</sup>C NMR

Solid-state <sup>15</sup>N and <sup>13</sup>C NMR was performed on the nitrogen-doped carbon overlayers synthesized from selectively isotope-labeled precursors. <sup>13</sup>C- and <sup>15</sup>N-labeled samples of 300 and 600 NC/SBA-15 were synthesized from melamine-(triamine-

15N3) (Sigma-Aldrich, 80-90% <sup>15</sup>N in triamine, 10-20% in triazine) and <sup>13</sup>C-enriched glucose (U-<sup>13</sup>C, 99%, Cambridge Isotope Laboratories). <sup>13</sup>C-labeled samples were synthesized from <sup>13</sup>C-enriched melamine (Sigma-Aldrich, 99% <sup>13</sup>C, 95% purity). The NC/SBA-15 samples were packed into 4-mm outer-diameter zirconia rotors. <sup>13</sup>C and <sup>15</sup>N NMR spectra were recorded at 100 MHz and 40 MHz, respectively, on a Bruker DSX400 spectrometer. Nearly quantitative <sup>13</sup>C and <sup>15</sup>N spectra were measured under 14-kHz magic angle spinning (MAS) and high-power <sup>1</sup>H decoupling, using composite-pulse multiCP<sup>42, 43</sup> with 2-s recycle and ten 0.3-s repolarization delays. Nearly quantitative spectra of nonprotonated carbon or mobile segments were obtained by using 68  $\mu$ s of recoupled dipolar dephasing before detection,<sup>44</sup> while the spectra of nonprotonated <sup>15</sup>N and <sup>13</sup>C multiple bonds away from <sup>1</sup>H were obtained from long-range recoupled <sup>1</sup>H dipolar dephasing.<sup>45</sup> To identify protonated and nonprotonated carbons from glucose linked by a bond, two-dimensional (2D) exchange with protonated and nonprotonated spectral editing (EXPANSE) NMR spectra<sup>46</sup> were recorded with a mixing time of 10 ms. To identify the proximity of different carbons originating from melamine in 300NC/SBA-15, a double-quantum/single-quantum (DQ/SQ) spectrum<sup>46</sup> of the sample synthesized from <sup>13</sup>C-melamine was measured. A <sup>1</sup>H-<sup>13</sup>C heteronuclear correlation spectrum<sup>47</sup> was also recorded from this sample to elucidate the fate of melamine. To select the signal of <sup>13</sup>C near <sup>15</sup>N in 300NC/SBA-15, <sup>13</sup>C detected rotational-echo double-resonance (REDOR) spectra with 5 rotation periods of recoupling were recorded after multiCP. After selecting the magnetization of <sup>13</sup>C near <sup>15</sup>N, 1-s spin-diffusion was performed to demonstrate that the nitrogen is uniformly mixed into the carbon film on the 3-nm scale. To identify bonding between <sup>13</sup>C and <sup>15</sup>N in the doubly-labeled 300NC/SBA-15, 2D <sup>13</sup>C-<sup>15</sup>N HSQC spectra were measured at 7 kHz MAS with 6 rotation periods of <sup>13</sup>C-<sup>15</sup>N recoupling.<sup>48</sup> Corresponding spectra between <sup>13</sup>C and nonprotonated <sup>15</sup>N were collected after suppression of the signal of nitrogen

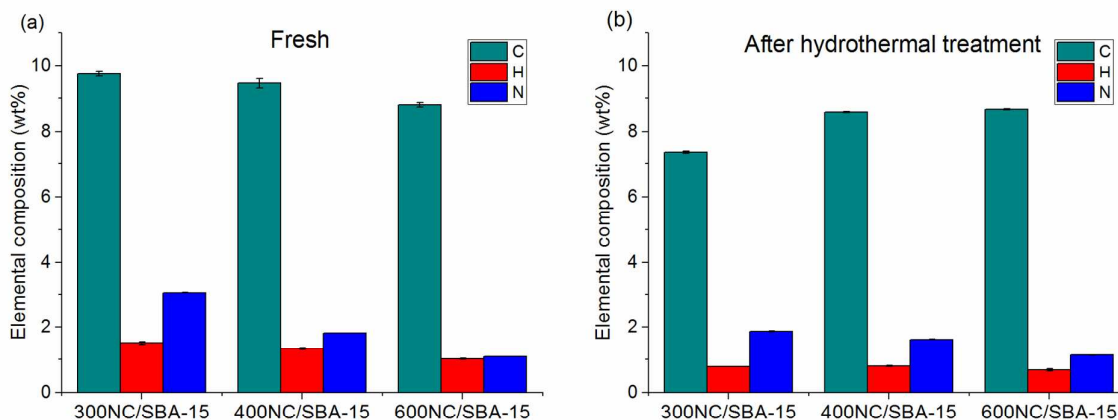


Fig. 1. Elemental analysis of NC/SBA-15 before (a) and after (b) 48 h hydrothermal treatment.

bonded to hydrogen by the recoupled  $^{15}\text{N}$ - $^1\text{H}$  dipolar interaction.<sup>48</sup>

## Results and discussion

### Characterization of nitrogen-doped carbon supports

Elemental analysis was performed on the three catalysts before and after 48 h hydrothermal treatment in water (Fig. 1). As the pyrolysis temperature increased, the carbon, hydrogen, and nitrogen content decreased, which was likely due to further condensation of the carbon coating. After the treatment, there was some loss of carbon, nitrogen and hydrogen, with 300NC/SBA-15 losing the most weight while 600NC/SBA-15 did not change appreciably. As discussed later in the NMR characterization, small amounts of incompletely pyrolyzed glucose and melamine remained on the 300NC/SBA-15, which was removed during treatment. It was likely that the weight change for the 400NC/SBA-15 was also due to incompletely pyrolyzed glucose and melamine. These unpyrolyzed species were not present in the higher temperature treated 600NC/SBA-15, so it had the least change in C and N content after hydrothermal treatment.

The surface area of three NC/SBA-15 materials also increased as the pyrolysis temperature increased (Table 1). As shown in Fig. S1, Type IV isotherms were observed, which indicated mesoporous structure for all three nitrogen-doped carbon materials. A H1 hysteresis was observed for all three fresh supports, indicating ordered cylinder-like pore structures as with the underlying SBA-15. After the 48 h hydrothermal treatment, the hysteresis changed to a H3 type. The pore size distributions of the materials before and after the

hydrothermal treatments are shown in Fig. S2. It was apparent that the mesoporous structure collapsed after hydrothermal treatment as evidenced by the pore size distribution curves as the pore size increased and the pore size distribution was broadened. Table 1 shows that both micropore and mesopore volumes decreased after hydrothermal treatment, with the 600NC/SBA-15 synthesized at higher temperature decreasing the least. Compared with just carbon coated SBA-15 (previously reported results<sup>12</sup>), the nitrogen-doped carbon coating provided less structural integrity to the base SBA-15 as the surface area of the C/SBA-15 only decreased around 10% after two 24 h hydrothermal treatments.<sup>12</sup> As will be shown below (through NMR characterization) the NC/SBA-15 materials contained significant amounts of pyridine, pyrimidine, pyrrole and amide groups. The nitrogen atoms in the C-N=C or C-NH-C groups have at least one less bond to carbon compared with graphitic carbon, which led to smaller condensation fragments and hence more water-exposed silica surface area. Therefore, the silica was hydrolyzed resulting in the collapse of the ordered mesoporous structure and a decrease in surface area. 300NC/SBA-15 lost the most surface area after the hydrothermal treatment while 600NC/SBA-15 lost the least. This trend was consistent with a more condensed carbon coating obtained from a higher pyrolysis temperature. Since 300NC/SBA-15 and 400NC/SBA-15 contained small amounts of incompletely pyrolyzed glucose and melamine species (confirmed by NMR later), these species dissolved more easily into the aqueous solution, thereby leaving some of the  $\text{SiO}_2$  surface unprotected. As a result, the Si-O-Si bond was hydrolyzed by water to Si-OH groups.<sup>49</sup> As a point of comparison, nitrogen-doped carbon coated 300NC/silica gel and 300NC/CMK-3 were also prepared. The

Table 1. BET surface area, pore volume and average pore diameter of supported NC materials before and after hydrothermal treatment.

Sample name		BET surface area (m <sup>2</sup> /g)	Total pore volume (cm <sup>3</sup> /g)	t-Plot micropore volume (cm <sup>3</sup> /g)	Mesopore volume (cm <sup>3</sup> /g)	BJH adsorption avg pore diameter (nm)
300NC/SBA-15	fresh	339	0.456	0.017	0.439	5.4
	48h HT <sup>a</sup>	94	0.251	0.006	0.245	10.7
400NC/SBA-15	fresh	351	0.459	0.026	0.433	5.2
	48h HT	147	0.260	0.011	0.249	7.1
600NC/SBA-15	fresh	365	0.468	0.031	0.437	5.1
	48h HT	235	0.371	0.019	0.352	6.3
300NC/silica gel	fresh	261	0.420	0.017	0.403	7.0
	48h HT	119	0.308	0.012	0.296	14.2
300NC/CMK-3	fresh	325	0.381	0.000	0.381	4.5
	48h HT	494	0.515	0.000	0.515	4.2

a: HT stands for 48 h of hydrothermal treatment in water at 170 °C.

Table 2. Dispersion and particle size of Pd NC/SBA-15 from CO chemisorption before and after hydrothermal treatment, and leached Pd percentage during hydrothermal treatment

Sample name	Fresh		48 h HT		Pd leached during HT %
	Dispersion%	Particle size/nm	Dispersion%	Particle size/nm	
Pd 300C/SBA-15 <sup>a</sup>	38	2.9	17	6.5	12.130
Pd 400C/SBA-15 <sup>a</sup>	32	3.5	15	7.3	9.060
Pd 600C/SBA-15 <sup>a</sup>	28	4.1	9	12.0	0.550
Pd 300NC/SBA-15	38	2.9	27	4.1	0.005
Pd 400NC/SBA-15	44	2.6	34	3.3	0.000
Pd 600NC/SBA-15	63	1.8	37	3.1	0.000
Pd 300NC/silica gel	26	4.3	22	5.2	NA

<sup>a</sup> For Pd C/SBA-15 materials, 48 h of HT (hydrothermal treatment) was performed by two consecutive 24 h hydrothermal treatments.<sup>12</sup>

BET surface area, physisorption isotherm, and pore size distribution of the 300NC/silica gel after hydrothermal treatment showed a similar trend as for 300NC/SBA-15. Conversely, the BET surface area of 300NC/CMK-3 increased after hydrothermal treatment and, within error, the BJH average pore diameter remained unchanged. This trend was also seen for carbon coated alumina

and silica, resulting in an increase in surface area after a shorter hydrothermal treatment period.<sup>10</sup> As shown in Fig. S2, the pore size distribution for 300NC/CMK-3 did not change after hydrothermal treatment and, within error, the BJH average pore diameter remained unchanged.

While it was apparent that use of a nitrogen-doped carbon

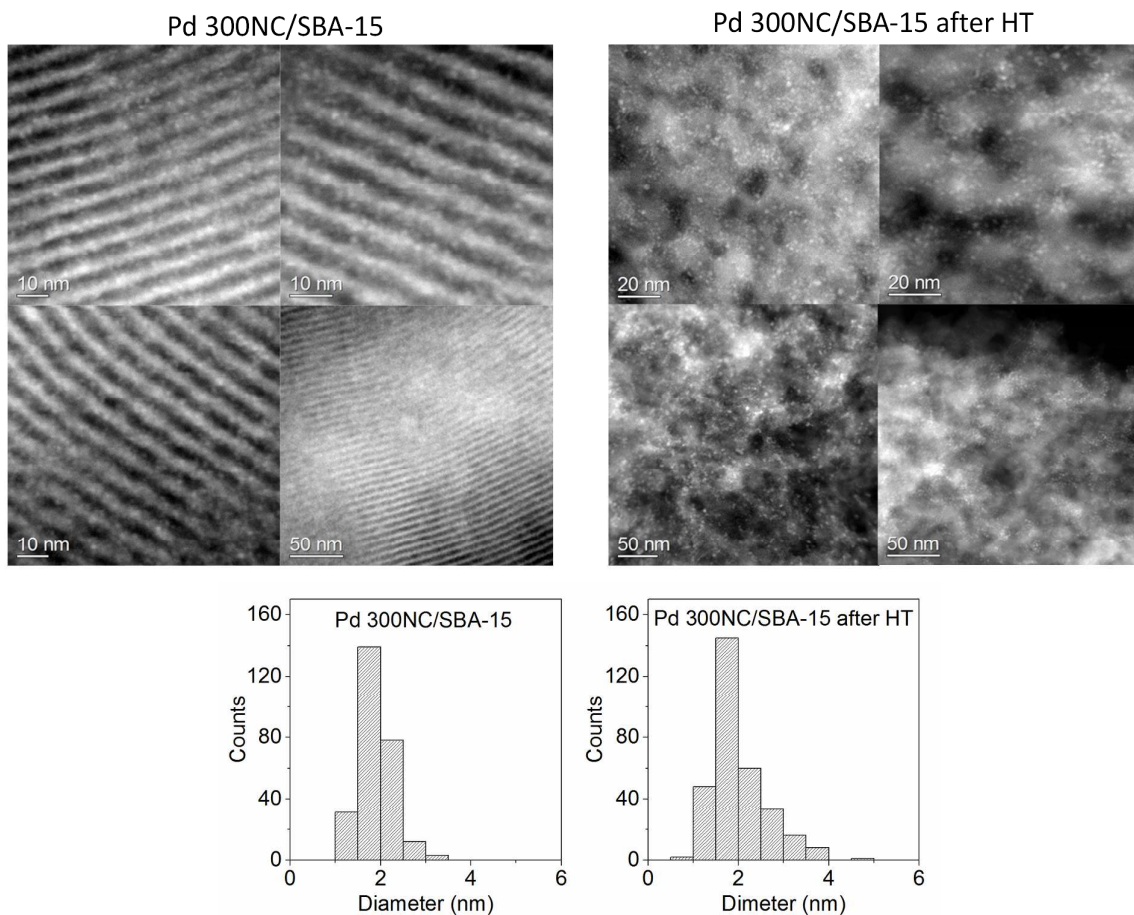


Fig. 2. HAADF-STEM images (top) and particle size distribution (bottom) of Pd 300NC/SBA-15 before and after 48 h hydrothermal treatment at 170 °C.

coating did not provide the same hydrothermal protection for the underlying silica support as did carbon coating, the primary goal of the study was to determine if introducing the nitrogen heteroatoms influenced the hydrothermal stability of Pd particles on the support. Therefore, the materials were also tested after Pd impregnation. CO chemisorption and HAADF-STEM were performed on the catalysts before and after the 48 h hydrothermal treatment. As shown in Table 2, CO chemisorption revealed that the dispersions of the Pd NC/SBA-15 catalysts were generally better than with the Pd C/SBA-15 materials. The Pd dispersion in all of the samples decreased after hydrothermal treatment, but to a significantly lesser extent for the Pd NC/SBA-15s than for the Pd C/SBA-15s. Additionally, ICP-OES data showed that leaching of Pd from the NC/SBA-15 materials into the solution during hydrothermal treatment was negligible, while it was significant for the C/SBA-15 materials.

HAADF-STEM images (Fig. 2) show that Pd particles were well dispersed on the fresh 300NC/SBA-15. After the 48 h hydrothermal treatment, the ordered mesoporous silica structure collapsed, in accordance with the decreased BET surface area and drastic change in pore size distribution. Interestingly, the Pd particles were still well-dispersed, with the STEM surface-weighted average Pd particle diameter

increasing only slightly, from 2.0 nm to 2.4 nm. In contrast, Pd on C/SBA-15 sintered to form much bigger particles after two 24 h hydrothermal treatments.<sup>12</sup>

To investigate the nitrogen functional groups of the Pd NC/SBA-15, XPS was performed on the material. Silicon at 103.4 eV was used to calibrate the spectra. Metallic Pd was found on all three NC/SBA-15 supported Pd catalysts from the Pd 3d XPS spectra (Fig. S3). Fig. 3 shows the N1s spectra, in which pyridinic N was assigned at 398.5 eV, pyrrolic N at 400.1 eV, and graphitic N at 401.4 eV.<sup>24, 28</sup>

The nitrogen content decreased with increasing pyrolysis temperature in accordance with elemental analysis. As the pyrolysis temperature increased, both the pyridinic and pyrrolic nitrogen groups decreased according to Fig. 3. There was a small amount of a graphitic N species in 600NC/SBA-15. Previously, C1s has been used to characterize different C-containing functional groups.<sup>50</sup> However, distinguishing between the many carbon ( $sp^2$  carbon and  $sp^3$  carbon, C=O, COOH, C-O, C=C-O, C=C-N, C=N, C-N) functional groups on the carbon surface in the current materials was beyond the resolution of the XPS instrument. As a result, NMR was used to analyze the carbon surface chemistry and its changes with synthesis temperature and hydrothermal treatment.

#### NMR characterization

To provide structural information on the NC coatings,

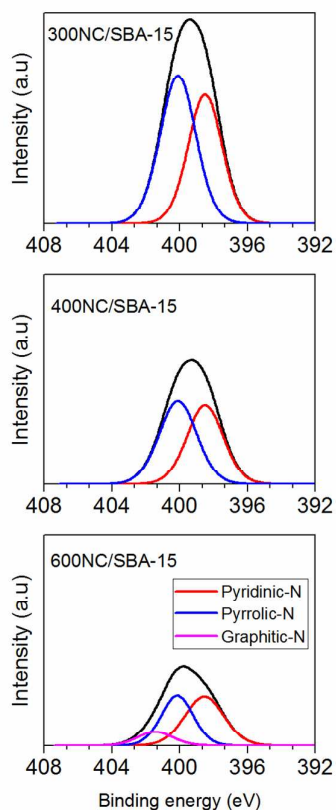


Fig. 3. N1s XPS spectra of Pd NC/SBA-15, normalized to the same scale.

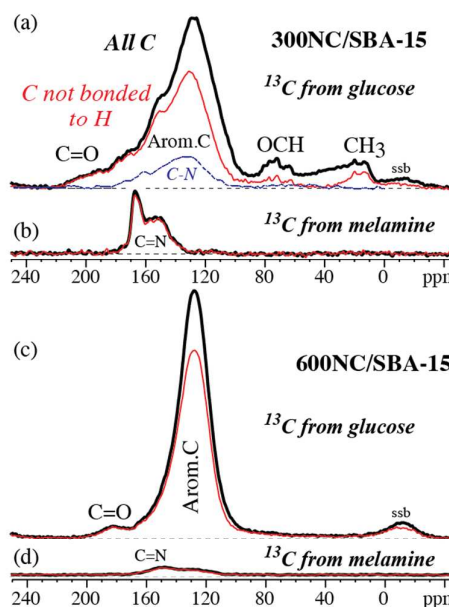


Fig. 4. Quantitative  $^{13}\text{C}$  NMR spectra of (a, b) 300NC/SBA-15 and (c, d) 600NC/SBA-15. (a, c) Signal of carbon derived from  $^{13}\text{C}_6$ -glucose; (b, d) signal of carbon derived from  $^{13}\text{C}_3$ -melamine, corrected for a minor background from natural-abundance  $^{13}\text{C}$  in glucose. Spectra of all carbons: bold black line; spectra of nonprotonated carbons and mobile groups: thin red line; spectra of carbon bonded to nitrogen: dashed blue line. The deconvolution of the latter spectra, which was obtained by  $^{13}\text{C}$  REDOR<sup>48</sup>, is presented in Fig. 6 below. "ssb": spinning sideband.

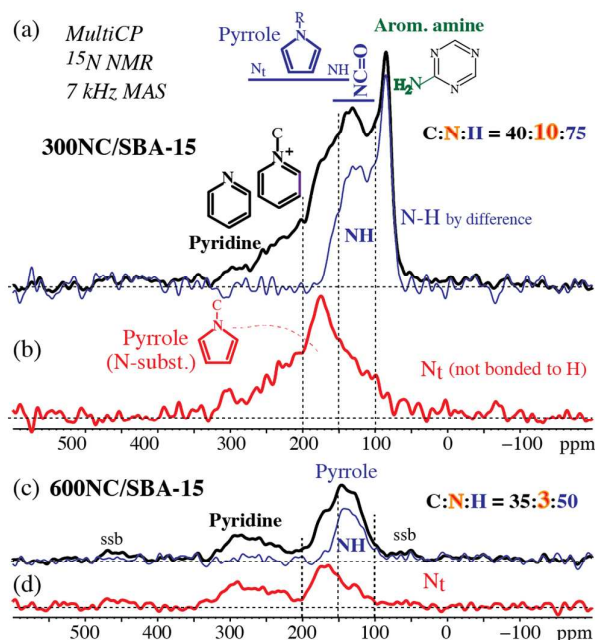


Fig. 5. MultiCP  $^{15}\text{N}$  NMR spectra of (a, b) 300NC/SBA-15 and (c, d) 600NC/SBA-15 made from unlabeled glucose and  $(^{15}\text{NH}_2)_3$ -labeled melamine. (a, c) Top trace (black): full spectrum; bottom trace (thin, blue): spectra of NH, obtained by dipolar-dephasing difference. (b, d): Spectra after dipolar dephasing, with signals of nonprotonated N (tertiary, N<sub>t</sub>).

quantitative  $^{13}\text{C}$  NMR spectra of 300 and 600NC/SBA-15 were recorded, see Fig. 4, with and without selection of carbons not bonded to H. Matching  $^{13}\text{C}$  NMR spectra of nominally equivalent materials with and without  $^{13}\text{C}$  enrichment, see Fig. S8, confirmed the reproducibility of the synthesis. A deconvolution of the  $^{13}\text{C}$  NMR spectrum of 300NC/SBA-15 in terms of functional groups is shown in Fig. S9. The spectra derived from  $^{13}\text{C}$ -enriched glucose, see Fig. 4a and c, quite closely resembled those of the corresponding carbon materials made without melamine. This was also confirmed in  $^{13}\text{C}$ - $^{13}\text{C}$  correlation spectra of materials made at 300 °C, see Fig. S10, which showed signals of furan and arene rings as well as C=O and COO groups bonded to  $\text{CH}_2$  and  $\text{CH}_3$  groups. On the other hand, the signals of melamine-derived carbon in Fig. 4b and d were quite distinctive, reflecting continued bonding of these carbons to nitrogen.

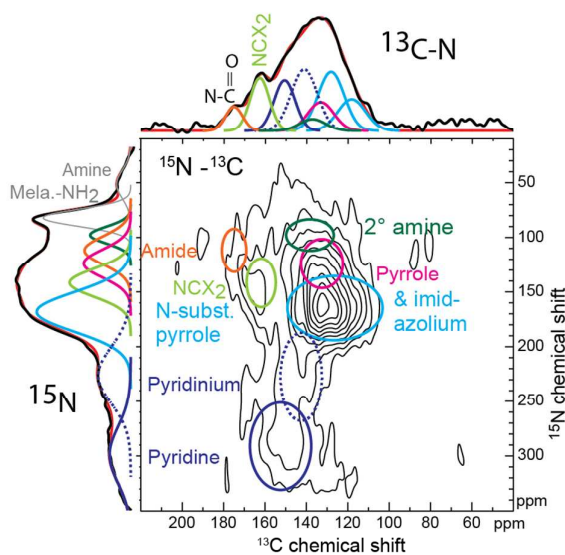


Fig. 6. Correlated deconvolution of  $^{13}\text{C}$  (top) and  $^{15}\text{N}$  (left) spectra of 300NC/SBA-15, based on 2D  $^{15}\text{N}$ - $^{13}\text{C}$  correlation (center). The deconvoluted  $^{15}\text{N}$  spectrum along the vertical axis is a 2:1 average of the multiCP spectrum and the projection of the 2D spectrum onto the  $^{15}\text{N}$  axis, which partly compensates for enhanced intensity of  $\text{NH}_n$  in the multiCP and  $\text{NC}_2$  in the  $^{15}\text{N}$ - $^{13}\text{C}$  spectrum. The signals of various functional groups are color coded. The concentrations derived from the analysis are compiled in Table 3.

For the performance of the materials, knowledge of the chemical forms of nitrogen in the NC coatings was of particular interest. This was studied by advanced multinuclear ( $^{15}\text{N}$ ,  $^{13}\text{C}$ , and  $^1\text{H}$ ) solid-state NMR on variously isotope-labeled materials, with a focus on 300NC/SBA-15. Tracing the fate of the carbons of melamine using 300NC/SBA-15 made from  $^{13}\text{C}$ -melamine, it was found that the melamine (i.e. triazine,  $\text{C}_3\text{N}_3$ ) rings contributed 7% of all C (compared with 13% in the melamine-glucose reactant mixture) and remained mostly intact after pyrolysis at 300 °C: Most  $^{13}\text{C}$  derived from melamine resonated in a fairly narrow range between 145 and 170 ppm, see Fig. 4b, showing that it was still  $\text{sp}^2$ -hybridized and bonded to three nitrogen atoms or two N and an O atom. This implied that a significant fraction of the nitrogen remained in the nonprotonated triazine form. On the other hand,  $^{15}\text{N}$  NMR of 300NC/SBA-15 made from  $(^{15}\text{NH}_2)_3$ -labeled melamine, see Fig. 5 and 6, showed that most

Table 3.  $^{15}\text{N}$ - $^{13}\text{C}$  REDOR NMR analysis of 300NC/SBA-15

	Pyridine	Pyridinium	N-subst. pyrrole & imidazolium	Imide	Pyrrole N-H	Amide	2° amine	Mela. -NH <sub>2</sub>	Amine
$^{13}\text{C}^*$	12%	18%	28%	11%	9%	5%	3%	N. D.	N. D.
$^{15}\text{N}$	9%	13%	27%	13%	10%	10%	5%	11%	3%

\*: Since melamine-NH<sub>2</sub> is not bonded to  $^{13}\text{C}$  from labeled glucose, it did not show up in the REDOR 2D spectrum. The total percentage of  $^{13}\text{C}$  in the table is renormalized to 86%. N. D.: not determined.

Table 4. Fresh vs. hydrothermally treated NC/SBA-15,  $^{13}\text{C}$  NMR analysis

$^{13}\text{C}$	Ket-one	Amide & COO	$\alpha\text{-XC}$	Nonp. Arene & NC	Nonp. $\beta\text{-XC}$	Prot. Arene	Prot. $\beta\text{-XC}$	OCH <sub>n</sub>	CH <sub>n</sub> & NCH <sub>n</sub>	CH <sub>3</sub>
300 NC	4%/3%	9%/8%	12%/10%	28%/~27%*	12%/~10%*	10%/~9%*	9%/~7%*	6%/1%	5%/3%	5%/3%
600 NC	4%/6%(2.5% of amide)		13%/12%	74%/73%		9%/9%		~0%/~0%		

Each double entry in the table is the percentage of the functional group in the fresh sample vs. the corresponding sample after hydrothermal treatment. The total percentage of the sample after hydrothermal treatment is referenced to the fresh sample.

\*: Not fully resolved, estimated.

Table 5. Fresh vs. hydrothermally treated NC/SBA-15, NMR analysis of  $^{13}\text{C}$  bonded to  $^{15}\text{N}$ 

$^{15}\text{N}$ <sup>1</sup>	Pyridine	Pyridinium	N-subst. pyrrole & imidazolium	Imide	Pyrrole N-H	Amide	2° amine	Mela.-NH <sub>2</sub>	Amine
300°C	5%/5%	13%/9%	22%/14%	12%/13%	12%/11%	10%/5%	7%/2%	17%/5%	2%/2%
600°C	30%/30%		38%/38%	~0%/~0%	32%/32%	~0%/~19% <sup>2</sup>	~0%/~0%		

Each entry in the table is the percentage of the functional group in the fresh sample vs. the corresponding sample after hydrothermal treatment. The total percentage for the sample after hydrothermal treatment (66% at 300°C, 119% at 600°C) is referenced to the fresh sample.

<sup>1</sup>: This table is for comparison between the fresh and hydrothermally-treated samples only, due to under-estimation of non-protonated  $^{15}\text{N}$  in  $^1\text{H}\text{-}^{15}\text{N}$  cross polarization (CP). A more quantitative estimation is given in Table 3.

<sup>2</sup>: The amide appears to undergo a net increase in  $^{15}\text{N}$ . However, it might be due to a highly proton-deficient environment of  $^{15}\text{N}$  converted to amide, making it less visible in CP.

of the NH<sub>2</sub> nitrogen of melamine had undergone a wide variety of chemical transformations, as expected in a Maillard reaction between an amine compound and glucose, a reducing sugar.<sup>48</sup> This result was also consistent with the decreased peak intensities of glucose-like species at 60-90 ppm in Fig. 4a compared with just carbon-coated SBA-15 material.<sup>12</sup> Only about 11% of the NH<sub>2</sub> remained in the primary amine form, giving rise to fairly sharp peaks at the edges (right and left, respectively) of the  $^{15}\text{N}$  and  $^{13}\text{C}$  spectra of the correspondingly isotope-labeled melamine, see Fig. 5 and 4b. As expected, the  $^{15}\text{N}\text{-}^{13}\text{C}$  correlation NMR spectrum of 300NC/SBA-15 made from  $^{13}\text{C}$ -glucose and ( $^{15}\text{NH}_2$ )<sub>3</sub>-labeled melamine, Fig. 6, lacked the NH<sub>2</sub> resonance at 90 ppm in the  $^{15}\text{N}$  spectrum since the amine group of melamine is not bonded to any glucose-derived carbon.

The various forms of nitrogen formed from the NH<sub>2</sub> groups of melamine have been identified by  $^{15}\text{N}$  NMR spectra with spectral editing shown in Fig. 5 and by  $^{15}\text{N}\text{-}^{13}\text{C}$  2D NMR with and without dipolar dephasing (Fig. 6 and S11); their amounts were estimated by simultaneous deconvolution of  $^{15}\text{N}$  and  $^{13}\text{C}$  spectra<sup>48</sup> (see Fig. 6). Data for 600NC/SBA-15 are shown in Fig. S12.  $^1\text{H}\text{-}^{13}\text{C}$  NMR and  $^{13}\text{C}\text{-}^{13}\text{C}$  correlation of  $^{13}\text{C}$  derived from  $^{13}\text{C}_3$ -melamine (Fig. S13 and S14) was also taken into account. Overall, 12-14% of all glucose-derived carbons were bonded to nitrogen (see Fig. 4a and S9).

In 300NC/SBA-15, the major form of nitrogen (ca. 27%) was substituted N of pyrrole or imidazolium resonating near 170

ppm. The next abundant form (ca. 13%) was pyridinium, visible as a broad shoulder around 220 ppm in Fig. 5b and 6, and merging with the pyridine/pyrimidine band (~10%), which extends out to 320 ppm. The pyridinium nitrogen presumably remained bonded to melamine. Amide and NCX<sub>2</sub> groups occurred with around 10% abundance each. Their N was mostly bonded to hydrogen. NCX<sub>2</sub> groups with a distinctive  $^{13}\text{C}$  resonance near 160 ppm contain sp<sup>2</sup>-hybridized carbon bonded to nitrogen and two other heteroatoms, of which one was double-bonded. Ureido (N<sub>2</sub>C=O) and, less likely, guanidino (N<sub>2</sub>C=N) groups are examples.<sup>51</sup> The ~160 ppm  $^{13}\text{C}$  and 130-160 ppm  $^{15}\text{N}$  chemical shifts also match those of cyclic amides with a bond to another sp<sup>2</sup>-hybridized carbon, for instance in uracil.<sup>51</sup> A detailed analysis of these spectra is provided in the Supporting Information. While only pyridine, pyrrole and graphitic nitrogen groups were identified by XPS, NMR provided a better resolution of the functional groups including both nitrogen and oxygen moieties groups.

Equilibration of  $^{13}\text{C}$  magnetization originating from carbons bonded to nitrogen within 1 s of  $^{13}\text{C}$  spin diffusion (see Fig. S15) showed that the nitrogen-containing structures were mixed with the furan, arene, and alkyl segments (but not with most of the untransformed OCH) on a <3-nm scale.

In the 600NC/SBA-15 material, the  $^{13}\text{C}$  and  $^{15}\text{N}$  NMR signals overall were strongly reduced (see Fig. 4d and 5c). The fraction of carbon from melamine was reduced to 2%, and the nitrogen derived from NH<sub>2</sub> was lower than in 300NC/SBA-15 by a factor

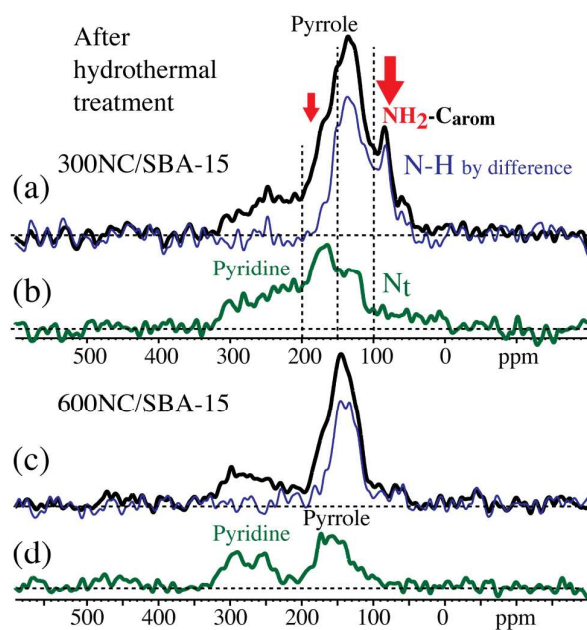


Fig. 7. MultiCP  $^{15}\text{N}$  NMR spectra of (a, b) 300NC/SBA-15 and (c, d) 600NC/SBA-15 made from  $(^{15}\text{N}\text{H}_2)_3$ -labeled melamine, after hydrothermal treatment. (a, c) Top trace (black): Full spectrum; bottom trace (thin, blue): Spectra of NH, obtained by dipolar-dephasing difference. (b, d): Spectra after dipolar dephasing, with signals of nonprotonated nitrogen (tertiary, Nt). Red arrows mark signals that have been reduced significantly by the hydrothermal treatment.

of  $\sim 4$ . Pyridine and pyrrole remained most prominent, while  $\text{NH}_2$  and pyridinium had been preferentially lost.

Fig. 7 shows the  $^{15}\text{N}$  NMR spectra of 300 and 600 NC/SBA-15 after hydrothermal treatment. Comparison with the spectra in Fig. 5 demonstrates a partial loss of  $\text{NH}_2$  and pyridinium in 300NC/SBA-15, while little change was seen for 600NC/SBA-15. The loss of nitrogen species in 300NC/SBA-15 and little loss in 600NC/SBA-15 was also confirmed by the elemental analysis after hydrothermal treatment, as 300NC/SBA-15 lost about

1/3 of the nitrogen while 600NC/SBA-15 did not lose a significant amount of nitrogen species. The changes in carbon and nitrogen functional groups after hydrothermal treatment are summarized in Tables 4 and 5. The data in Table 4 show a slight decrease in carbon functional groups on 300NC/SBA-15 after hydrothermal treatment, in accordance with elemental analysis, where carbon percentage dropped from 9.77% to 7.34%. On the other hand, 600NC/SBA-15 showed a much smaller decrease in carbon functional groups as the carbon percentage in the elemental analysis changed only from 8.80% to 8.67%.

The improved hydrothermal stability of Pd NC/SBA-15 was closely correlated with nitrogen doping. Pyridine, pyrrole and imidazolium groups helped to improve the hydrothermal stability of Pd particles since both 300NC/SBA-15 and 600NC/SBA-15 showed better stability than 300C/SBA-15 and 600C/SBA-15, as discussed in the next section. Further, the pyridine and pyrrole contents in both 300NC/SBA-15 and 600NC/SBA-15 remained unchanged after hydrothermal treatment. There was some decrease in amide, secondary amine, and melamine content in 300NC/SBA-15, which was likely due to dissolution of unpyrolyzed melamine-like species during the hydrothermal treatment (Table 5). However, as the Pd particle size did not change much and negligible leaching was observed on Pd 300NC/SBA-15, it seems likely that the Pd particles were not anchored on these less stable nitrogen functional groups. The nitrogen functional groups in 600NC/SBA-15 did not change much after hydrothermal treatment. Furthermore, as 300NC/SBA-15 showed better stability in conversion than 600NC/SBA-15 (see below), it was likely that synergistic effects between nitrogen and oxygen heteroatoms induced the extra stability on 300NC/SBA-15 as there were significantly more oxygen-containing functional groups in the carbon coating.

#### Hydrothermal reaction data

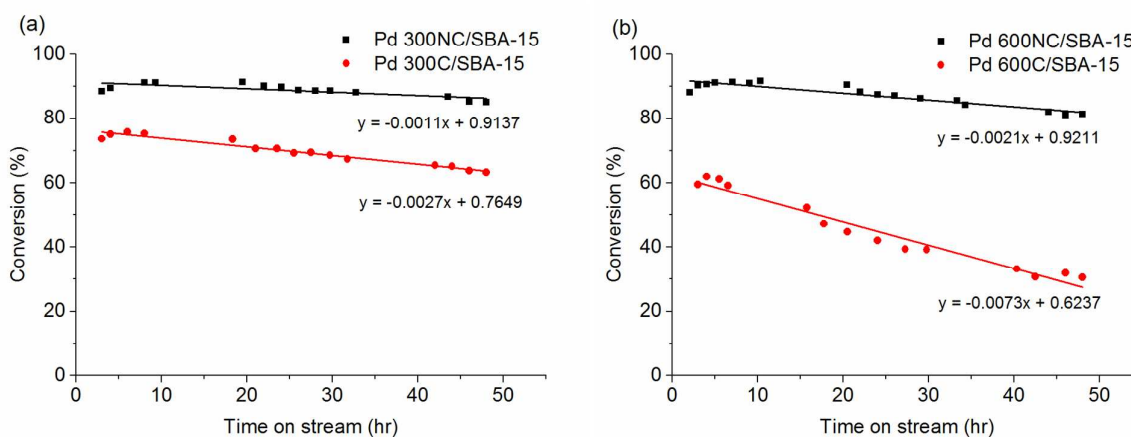


Fig. 8. Furfural hydrogenation (a) Pd 300NC/SBA-15, Pd 300C/SBA-15, (b) Pd 600NC/SBA-15, Pd 600C/SBA-15, at  $130^\circ\text{C}$ , 750 psi for 48 h

Fixed-bed continuous flow reaction of aqueous-phase hydrogenation (APH) of furfural was used as a probe reaction to test the stability of the catalyst at 130 °C and 750 psi for 48 h, see catalytic data in Fig. 8. All of the Pd NC/SBA-15 catalysts showed both better activity and stability than the Pd C/SBA-15 catalysts. The better activity of Pd NC/SBA-15 could be attributed to smaller Pd particles, as indicated by both CO chemisorption in Table 2 and HAADF-STEM analysis in Fig. 9 and Table 6. The incorporation of nitrogen helped to improve the dispersion of Pd particles, which was likely due to the strong interaction between Pd particles and nitrogen functional groups.<sup>25, 27, 52</sup> It appeared that this strong

interaction also greatly diminished sintering of the metal particles. This effect was demonstrated with better stability of Pd NC/SBA-15 compared with Pd C/SBA-15. As reported previously, Pd 300C/SBA-15 gave better activity and stability than Pd 600C/SBA-15, suggesting that the low-temperature synthesized carbon with its more oxygen functional groups allowed for better dispersion and stabilization of the Pd particles.<sup>12</sup> Pd 300NC/SBA-15 also showed better stability than the higher temperature Pd 600NC/SBA-15 as the deactivation rate of Pd 300NC/SBA-15 was about half that of Pd 600NC/SBA-15. Importantly, less than 1% of the total Pd leached into the reaction solution for all four catalysts, as

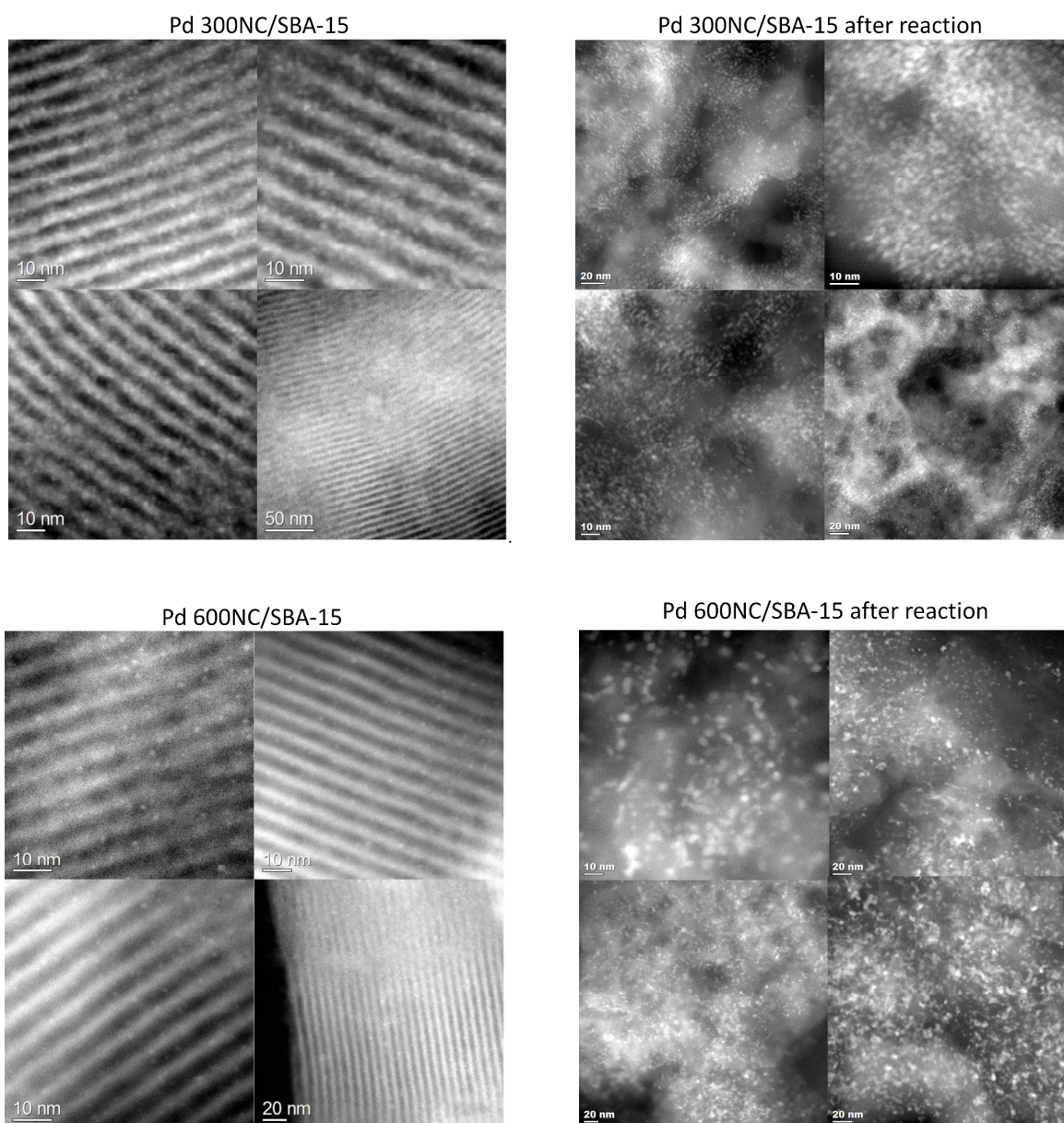


Fig. 9. HAADF-STEM images of Pd 300NC/SBA-15, and Pd 600NC/SBA-15 before and after 48 h of reaction time-on-stream.

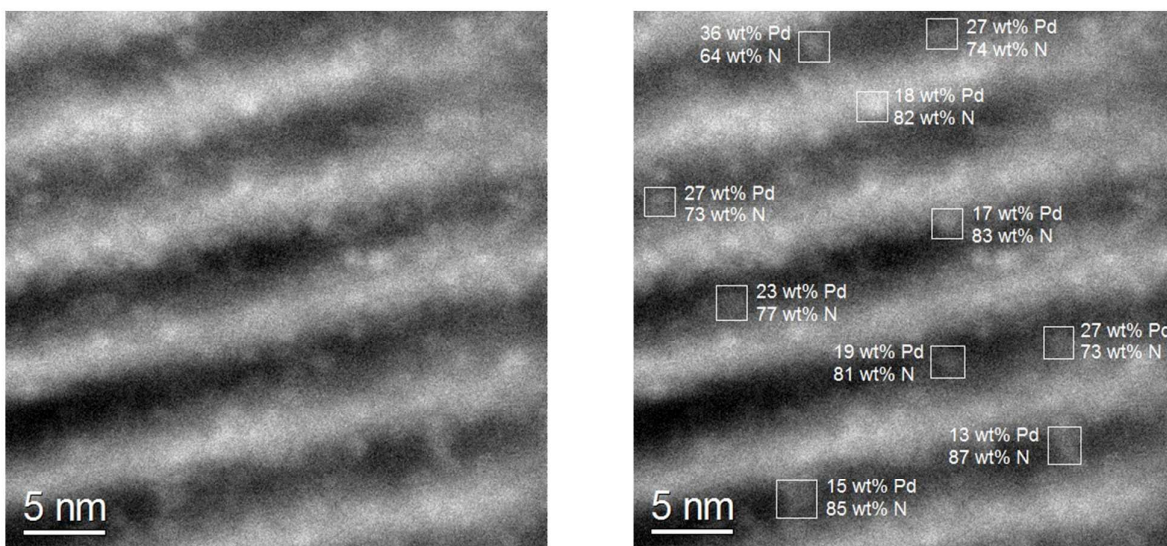


Fig. 10. HAADF-STEM image (left) and elemental compositions of individual Pd particles (right) for fresh Pd 300NC/SBA-15.

verified by ICP-OES.

Monitoring catalyst changes is indispensable in a stability study. Therefore, STEM analysis was performed on the Pd 300NC/SBA-15 and Pd 600NC/SBA-15 before and after 48 h of reaction (Fig. 9). As with the hydrothermal stability tests, the mesoporous structure collapsed for both 300NC/SBA-15 and 600NC/SBA-15 as the ordered cylindrical pores of SBA-15 disappeared. However, the Pd particles were still well dispersed. This result was surprising since previous work found that when the underlying oxide support lost its structural integrity, the metal phase significantly sintered.<sup>13</sup>

Sintering occurred to some extent in both catalysts, as indicated by the particle size data in Table 6 and particle size distribution in Fig. S4. More sintering was observed for the Pd

600NC/SBA-15 as the particle size increased from 2.2 nm to 4.0 nm while Pd 300NC/SBA-15 only slightly increased from 2.0 nm to 2.3 nm. To examine how fast the ordered mesoporous structure of SBA-15 was destroyed, STEM analysis was performed after a shortened reaction time (10 h). As shown in Fig. S5, some of the ordered mesoporous structure was intact at that time, suggesting a gradual destruction of the SBA-15 structure with time-on-stream. STEM-EDS analysis on fresh Pd 300NC/SBA-15 in Fig. 10 suggested that the Pd particles were anchored to nitrogen functional groups. This direct interaction between the nitrogen heteroatoms and Pd could be the reason that the Pd particles had minimal sintering even when the underlying silica support was hydrolyzed.

Previous research on hydrothermal reactions has shown that

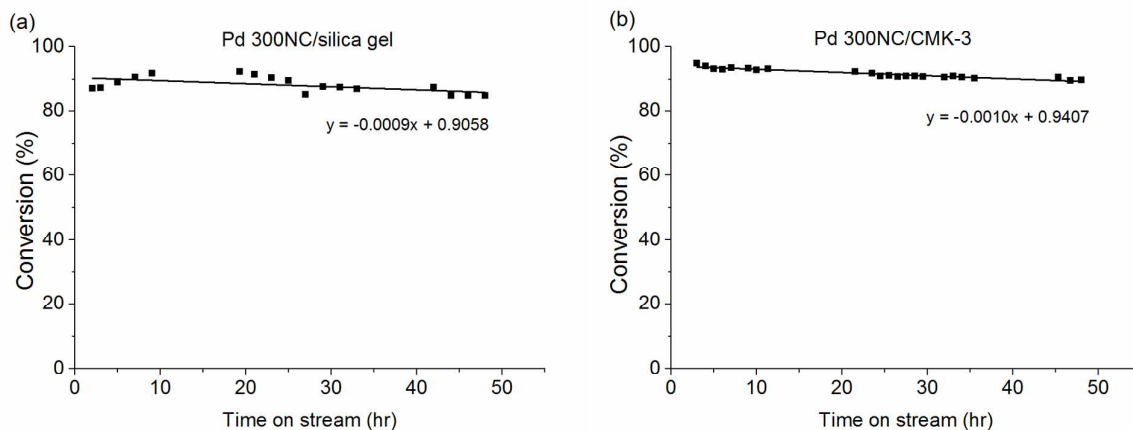


Fig. 11. Continuous flow hydrogenation of furfural on Pd 300NC/silica gel and Pd 300NC/CMK-3 at 130 °C, 750 psi for 48 h.

Table 6. Dispersion and particle size from CO chemisorption and STEM before and after 48 hr flow reaction.

Sample name	Fresh					After reaction		
	Dispersion <sup>a</sup> %	Particle size <sup>a</sup> /nm	STEM Particle diameter <sup>b</sup> /nm	Fraction of surface atoms <sup>c</sup> %	Initial reactivity <sup>d</sup> /s <sup>-1</sup>	STEM Particle diameter <sup>b</sup> /nm	Fraction of surface atoms <sup>c</sup> %	Ending reactivity <sup>d</sup> /s <sup>-1</sup>
Pd 300NC/SBA-15	38	2.9	2.0	55	0.0132	2.3	49	0.0145
Pd 600NC/SBA-15	63	1.8	2.2	52	0.0139	4.0	28	0.0233
Pd 300NC/silica gel	26	4.3	3.2	35	0.0185	3.2	35	0.0183
Pd 300NC/CMK-3	27	4.1	2.5	45	0.0158	2.7	41	0.0162
Pd 300C/SBA-15	38	2.9	3.1	36	0.0153	NA	NA	NA
Pd 600C/SBA-15	28	4.1	3.8	30	0.0154	NA	NA	NA

<sup>a</sup>; Data from CO chemisorption. <sup>b</sup>: Data from surface-weighted average diameter from STEM using  $\sum d^3 / \sum d^2$ . <sup>c</sup>: Fraction of surface atoms is calculated from  $1.12/d$  (measured by STEM). <sup>d</sup>: Initial and final overall reactivity per site were calculated by using the equation below; fraction of surface atoms from STEM was used as dispersion in the calculation.

$$\text{reactivity per site} = \frac{(\text{moles of reactant converted})}{\{(\text{moles of metal in catalyst}) \times (\text{dispersion}) \times (\text{reaction time})\}}$$

sintering was a common cause for deactivation rather than leaching.<sup>13, 53</sup> Bond et al. found Ru particles sintered to larger particles on Al<sub>2</sub>O<sub>3</sub>, TiO<sub>2</sub>, SiO<sub>2</sub>, and carbon at temperatures as low as 50 °C during aqueous hydrogenation of levulinic acid.<sup>54</sup> As evidenced here, nitrogen-doping of carbon appears to offer a promising approach for stabilizing Pd particles.

To further investigate the effect of the underlying support on stability, a nitrogen-doped carbon coating was synthesized on mesoporous silica gel, followed by 48 h hydrothermal treatment and continuous flow reaction. The 300NC/silica gel also lost more than half of its initial surface area during hydrothermal treatment (Table 1) and showed a much broader pore size distribution (Fig. S2). However, the Pd 300NC/silica gel as shown in Fig. 11 gave similar activity and stability in furfural conversion, compared with Pd 300NC/SBA-15. STEM analysis also revealed no change in average Pd particle size after reaction (Fig. S4 and S16).

As the SBA-15 and silica gel supports were hydrolyzed under hydrothermal conditions due to smaller carbon fragments from nitrogen incorporation, we further prepared a nitrogen-doped carbon coated CMK-3, an ordered mesoporous carbon material known to have hydrothermal stability. A similar retention of catalytic activity was observed on Pd 300NC/CMK-3 compared to Pd 300NC/silica gel (Fig. 11). The ordered mesoporous structure of CMK-3 was confirmed by STEM both before and after reaction for 48 h in Fig. S16, with little Pd sintering (Fig. S4).

Although the initial Pd particle sizes for the Pd 300NC/SBA-15, Pd 600NC/SBA-15, Pd 300NC/silica gel, and Pd 300NC/CMK-3 materials were different, the initial activity was similar (around 90% conversion). The initial and final overall reactivity of the catalyst were calculated as summarized in Table 6 below. These calculated values strongly suggest that the reaction was

mass-transfer limited as the furfural hydrogenation is quite fast with a Pd catalyst and the reactivity per site increased as the pore size increased during the hydrothermal reaction. While reaction conditions could have been selected to avoid mass transfer limitations by lowering the reaction temperature, an important goal of the study was to examine catalyst stability under hydrothermal conditions relevant to common aqueous phase reactions. The greater deactivation rate of Pd 600NC/SBA-15 than Pd 300NC/SBA-15 was likely due to its more significant Pd particle sintering. For Pd 300NC/silica gel and Pd 300NC/CMK-3, the overall reactivity per site remained unchanged throughout the reaction. The different reactivity per site induced by different particle size

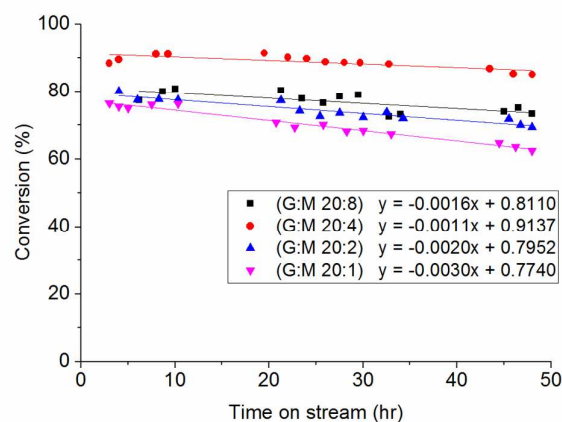


Fig. 12. Aqueous-phase hydrogenation of furfural for Pd 300NC/SBA-15 with different melamine contents. G stands for glucose and M stands for melamine.

Table 7. CO chemisorption dispersion and particle size of Pd 300NC/SBA-15 with different melamine content (G: glucose, M: melamine).

	Dispersion %	Particle size/nm
Pd 300NC/SBA15 (G:M 20:8)	33	3.4
Pd 300NC/SBA15 (G:M 20:4)	38	3.0
Pd 300NC/SBA15 (G:M 20:2)	33	3.4
Pd 300NC/SBA15 (G:M 20:1)	32	3.5

and potentially different metal-support interaction is not the focus of this paper.

#### The influence of nitrogen loading on hydrothermal stability

To study the effects of nitrogen loading on hydrothermal stability, Pd 300NC/SBA-15 materials were synthesized with different melamine loading while keeping the SBA-15 to glucose ratio the same. Table 7 shows the dispersion and particle size of Pd 300NC/SBA-15 with different amounts of nitrogen in the coating. In the reaction studies, the stability decreased when too little nitrogen was present in the coating (Fig. 12). The material with a melamine ratio of 20:4 gave the highest dispersion and the lowest activity loss during reaction.

#### Insights into the nitrogen-doped carbon coating on improved

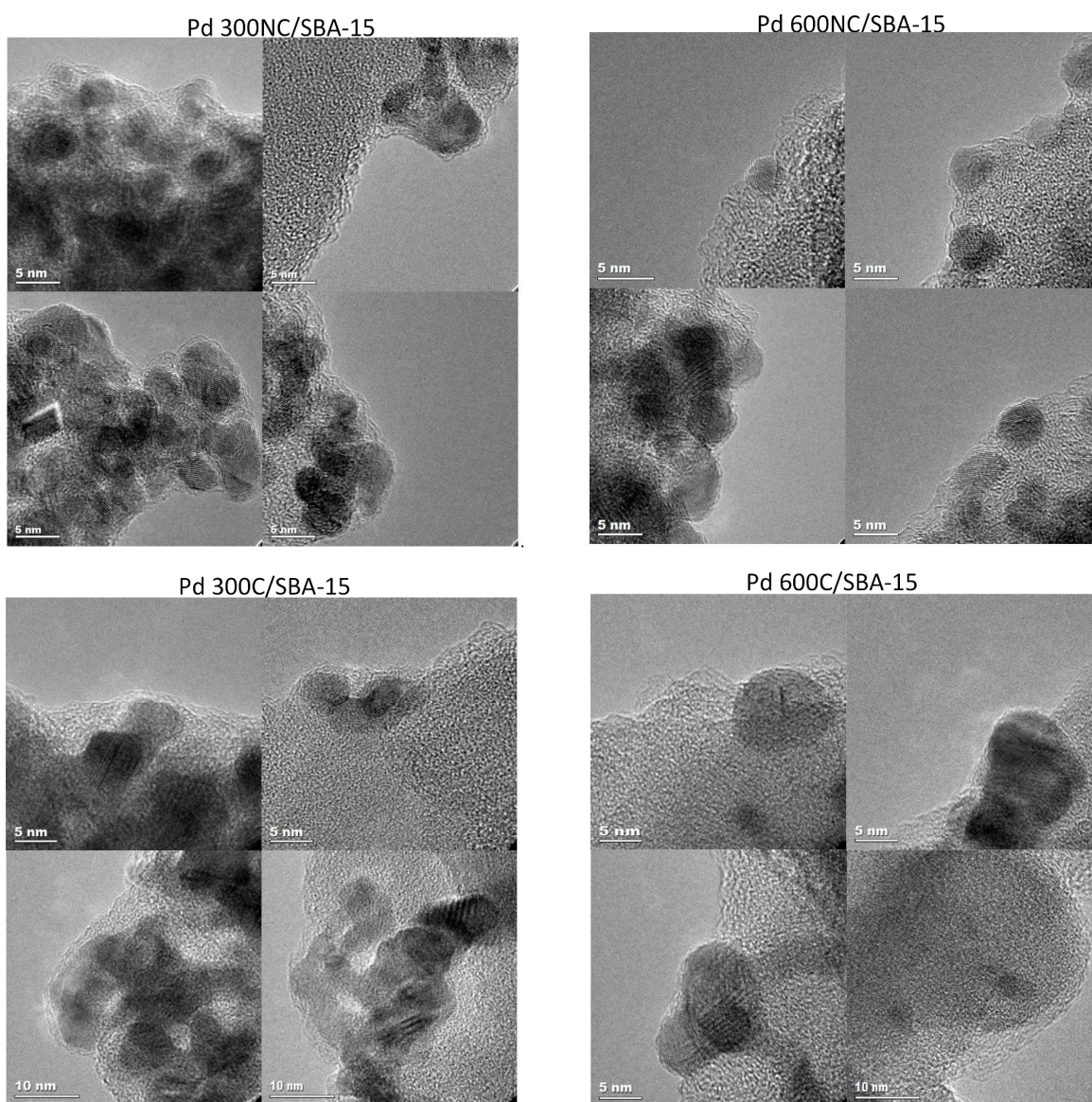


Fig. 13. HRTEM images of Pd 300NC/SBA-15 and Pd 600NC/SBA-15 (top); Pd 300C/SBA-15 and Pd 600C/SBA-15 (bottom) after 48 h of flow reaction.

### hydrothermal stability

HRTEM of the Pd 300NC/SBA-15 and Pd 600NC/SBA-15 after 48 h of reaction showed that the Pd particles were covered with a carbon protective overlayer. A thicker carbon overlayer was observed for the Pd 300NC/SBA-15 as seen in Fig. 13. Whereas, the carbon overlayer was significantly less for the Pd particles on Pd 600NC/SBA-15. Given the high reactivity of Pd 300NC/SBA-15 even after 48 h, it would appear that the carbon overlayer on the Pd particles was porous and did not block the active sites. The HRTEM images suggested that the carbon overlayer may help to protect the Pd particles from sintering and leaching under the hydrothermal conditions. The different thickness of the carbon overlayer on the Pd particles could have been due to the carbon coating on 300NC/SBA-15 being less condensed and containing more oxygen and nitrogen functional groups, which allowed for more mobility of the carbon relative to the more condensed carbon coating on 600NC/SBA-15. A similar trend was seen for the Pd 300C/SBA-15 and Pd 600C/SBA-15 materials as well. Given the enhanced stability of Pd 300NC/SBA-15 relative to Pd 300C/SBA-15, the apparent migration of some carbon over the Pd particles was not the only mechanism for stabilizing the Pd particles. Therefore, the presence of nitrogen heteroatoms in the coating layer was still an important contributor to the stability of the Pd 300NC/SBA-15 catalyst.

### Conclusions

Novel Pd NC/SBA-15 materials were synthesized and characterized extensively through HRTEM, HAADF-STEM, as well as  $^{13}\text{C}$  and  $^{15}\text{N}$  NMR before and after hydrothermal treatment and flow reaction conditions. These materials gave better hydrothermal stability of the Pd nanoparticles than carbon coated SBA-15 materials without nitrogen functional groups, as both leaching and sintering of the Pd were reduced. Better dispersion of the Pd particles was also observed for the nitrogen-doped materials. The lower temperature synthesized, Pd 300NC/SBA-15, which had more nitrogen and oxygen heteroatoms in the carbon coating, showed better stability than Pd 600NC/SBA-15. Unfortunately, the introduction of nitrogen into the carbon coating resulted in a less stable underlying silica support relative to the carbon-only coated SBA-15, as smaller carbon fragments resulting from nitrogen incorporation appeared to allow water to interact with the underlying silica, leading to structural collapse of the mesoporous silica structure under hydrothermal conditions. Remarkably, the stability of the Pd particles was not affected by hydrolysis of the silica. Similar testing with Pd 300NC/silica gel and Pd 300NC/CMK-3 demonstrated that the coating technique could be applied to other support materials as well, with the CMK-3 in particular being promising due to its intrinsic hydrothermal structural stability. Detailed  $^{15}\text{N}$  and  $^{13}\text{C}$  NMR characterization indicated that pyridine, pyrrole, and imidazolium groups helped to improve the hydrothermal stability of Pd particles. The particularly enhanced stability of 300NC/SBA-15 could have been due to both the presence of

oxygen and nitrogen functional groups in the carbon coating as well as the formation of a protective carbon overlayer on the Pd particles. The strategy of nitrogen doping into carbon material offers a new approach to improve the hydrothermal stability of supported metal catalyst under relevant biomass conversion conditions.

### Conflicts of interest

There are no conflicts to declare.

### Acknowledgements

This work is supported by the Center for Biorenewable Chemicals funded by NSF grant EEC-0813570. We would like to thank Dr. Dapeng Jing for XPS analysis, Dr. Yuan Xue for elemental analysis, and Dr. Patrick Johnston for ICP analysis. We also thank Professor Jean-Philippe Tessonnier for helpful discussions.

### References

1. D. M. Alonso, J. Q. Bond and J. A. Dumesic, *Green Chem.*, 2010, **12**, 1493-1513.
2. J. S. Luterbacher, D. M. Alonso and J. A. Dumesic, *Green Chem.*, 2014, **16**, 4816-4838.
3. G. W. Huber, S. Iborra and A. Corma, *Chem. Rev.*, 2006, **106**, 4044-4098.
4. J. N. Chheda, G. W. Huber and J. A. Dumesic, *Angew. Chem. Int. Ed.*, 2007, **46**, 7164-7183.
5. M. J. Climent, A. Corma and S. Iborra, *Green Chem.*, 2014, **16**, 516-547.
6. J.-P. Lange, *Angew. Chem. Int. Ed.*, 2015, **54**, 13186-13197.
7. H. Xiong, H. N. Pham and A. K. Datye, *Green Chem.*, 2014, **16**, 4627-4643.
8. T. J. Schwartz, B. J. O'Neill, B. H. Shanks and J. A. Dumesic, *ACS Catal.*, 2014, **4**, 2060-2069.
9. C. Sievers, Y. Noda, L. Qi, E. M. Albuquerque, R. M. Rioux and S. L. Scott, *ACS Catal.*, 2016, **6**, 8286-8307.
10. H. N. Pham, A. E. Anderson, R. L. Johnson, K. Schmidt-Rohr and A. K. Datye, *Angew. Chem. Int. Ed.*, 2012, **51**, 13163-13167.
11. H. Xiong, T. J. Schwartz, N. I. Andersen, J. A. Dumesic and A. K. Datye, *Angew. Chem. Int. Ed.*, 2015, **54**, 7939-7943.
12. J. Huo, R. L. Johnson, P. Duan, H. N. Pham, D. Mendivelso-Perez, E. A. Smith, A. K. Datye, K. Schmidt-Rohr and B. H. Shanks, *Catal. Sci. Technol.*, 2018, **8**, 1151-1160.
13. H. N. Pham, A. E. Anderson, R. L. Johnson, T. J. Schwartz, B. J. O'Neill, P. Duan, K. Schmidt-Rohr, J. A. Dumesic and A. K. Datye, *ACS Catal.*, 2015, **5**, 4546-4555.
14. H. N. Pham, Y. J. Pagan-Torres, J. C. Serrano-Ruiz, D. Wang, J. A. Dumesic and A. K. Datye, *Appl. Catal., A*, 2011, **397**, 153-162.
15. J. Z. Duan, Y. T. Kim, H. Lou and G. W. Huber, *Catal. Today*, 2014, **234**, 66-74.
16. Y. Qiu, J. J. Huo, F. Jia, B. H. Shanks and W. Z. Li, *J. Mater. Chem. A*, 2016, **4**, 83-95.
17. H. B. Wang, T. Maiyalagan and X. Wang, *ACS Catal.*, 2012, **2**, 781-794.

18. W. Ju, M. Favaro, C. Durante, L. Perini, S. Agnoli, O. Schneider, U. Stimming and G. Granozzi, *Electrochim. Acta*, 2014, **141**, 89-101.
19. L. Perini, C. Durante, M. Favaro, S. Agnoli, G. Granozzi and A. Gennaro, *Appl. Catal., B*, 2014, **144**, 300-307.
20. L. Perini, C. Durante, M. Favaro, V. Perazzolo, S. Agnoli, O. Schneider, G. Granozzi and A. Gennaro, *ACS Appl. Mater. Interfaces*, 2015, **7**, 1170-1179.
21. L. F. Chen, X. D. Zhang, H. W. Liang, M. G. Kong, Q. F. Guan, P. Chen, Z. Y. Wu and S. H. Yu, *ACS Nano*, 2012, **6**, 7092-7102.
22. Z. S. Ma, H. Y. Zhang, Z. Z. Yang, G. P. Ji, B. Yu, X. W. Liu and Z. M. Liu, *Green Chem.*, 2016, **18**, 1976-1982.
23. K. Chizari, I. Janowska, M. Houille, I. Florea, O. Ersen, T. Romero, P. Bernhardt, M. J. Ledoux and C. Pham-Huu, *Appl. Catal., A*, 2010, **380**, 72-80.
24. Z. L. Li, J. H. Liu, C. G. Xia and F. W. Li, *ACS Catal.*, 2013, **3**, 2440-2448.
25. Z. L. Li, J. L. Li, J. H. Liu, Z. L. Zhao, C. G. Xia and F. W. Li, *ChemCatChem*, 2014, **6**, 1333-1339.
26. Y. Wang, J. Yao, H. R. Li, D. S. Su and M. Antonietti, *JACS*, 2011, **133**, 2362-2365.
27. X. Xu, Y. Li, Y. T. Gong, P. F. Zhang, H. R. Li and Y. Wang, *JACS*, 2012, **134**, 16987-16990.
28. P. F. Zhang, Y. T. Gong, H. R. Li, Z. R. Chen and Y. Wang, *Nat. Commun.*, 2013, **4**.
29. W. Z. Shen and W. B. Fan, *J. Mater. Chem. A*, 2013, **1**, 999-1013.
30. Z. X. Wu, P. A. Webley and D. Y. Zhao, *J. Mater. Chem.* 2012, **22**, 11379-11389.
31. S. S. Feng, W. Li, Q. Shi, Y. H. Li, J. C. Chen, Y. Ling, A. M. Asiri and D. Y. Zhao, *Chem. Commun.*, 2014, **50**, 329-331.
32. Y. Wang, X. C. Wang and M. Antonietti, *Angew. Chem. Int. Ed.*, 2012, **51**, 68-89.
33. A. Thomas, A. Fischer, F. Goettmann, M. Antonietti, J. O. Muller, R. Schlogl and J. M. Carlsson, *J. Mater. Chem.*, 2008, **18**, 4893-4908.
34. X. H. Li, X. C. Wang and M. Antonietti, *Chem. Sci.*, 2012, **3**, 2170-2174.
35. M. Lezanska, P. Pietrzyk and Z. Sojka, *J. Phys. Chem. C*, 2010, **114**, 1208-1216.
36. G. Ertl, H. Knözinger and J. Weitkamp, *Handbook of Heterogeneous Catalysis*, Wiley, 2008.
37. D. Y. Zhao, J. L. Feng, Q. S. Huo, N. Melosh, G. H. Fredrickson, B. F. Chmelka and G. D. Stucky, *Sci.*, 1998, **279**, 548-552.
38. S. Jun, S. H. Joo, R. Ryoo, M. Kruk, M. Jaroniec, Z. Liu, T. Ohsuna and O. Terasaki, *JACS*, 2000, **122**, 10712-10713.
39. P. Canton, G. Fagherazzi, M. Battagliarin, F. Menegazzo, F. Pinna and N. Pernicone, *Langmuir*, 2002, **18**, 6530-6535.
40. G. Fagherazzi, P. Canton, P. Riello, N. Pernicone, F. Pinna and A. Battagliarin, *Langmuir*, 2000, **16**, 4539-4546.
41. B. J. O'Neill, D. H. K. Jackson, A. J. Crisci, C. A. Farberow, F. Shi, A. C. Alba-Rubio, J. Lu, P. J. Dietrich, X. Gu, C. L. Marshall, P. C. Stair, J. W. Elam, J. T. Miller, F. H. Ribeiro, P. M. Voyles, J. Greeley, M. Mavrikakis, S. L. Scott, T. F. Kuech and J. A. Dumesic, *Angew. Chem. Int. Ed.*, 2013, **52**, 13808-13812.
42. R. L. Johnson and K. Schmidt-Rohr, *J. Magn. Reson.*, 2014, **239**, 44-49.
43. P. Duan and K. Schmidt-Rohr, *J. Magn. Reson.*, 2017, **285**, 68-78.
44. J. D. Mao and K. Schmidt-Rohr, *Environ. Sci. Technol.*, 2004, **38**, 2680-2684.
45. J. D. Mao and K. Schmidt-Rohr, *J. Magn. Reson.*, 2003, **162**, 217-227.
46. R. L. Johnson, J. M. Anderson, B. H. Shanks, X. Fang, M. Hong and K. Schmidt-Rohr, *J. Magn. Reson.*, 2013, **234**, 112-124.
47. J. D. Mao, B. Xing and K. Schmidt-Rohr, *Environ. Sci. Technol.*, 2001, **35**, 1928-1934.
48. X. Fang and K. Schmidt-Rohr, *J. Agric. Food. Chem.*, 2009, **57**, 10701-10711.
49. R. A. Pollock, G. Y. Gor, B. R. Walsh, J. Fry, I. T. Ghampson, Y. B. Melnichenko, H. Kaiser, W. J. DeSisto, M. C. Wheeler and B. G. Frederick, *J. Phys. Chem. C*, 2012, **116**, 22802-22814.
50. S. Reiche, R. Blume, X. C. Zhao, D. Su, E. Kunkes, M. Behrens and R. Schloegl, *Carbon*, 2014, **77**, 175-183.
51. X. W. Fang, J. D. Mao, R. M. Cory, D. M. McKnight and K. Schmidt-Rohr, *Magn. Reson. Chem.*, 2011, **49**, 775-780.
52. S. S. Chen, P. Y. Qi, J. Chen and Y. Z. Yuan, *RSC Adv.*, 2015, **5**, 31566-31574.
53. O. A. Abdelrahman, A. Heyden and J. Q. Bond, *ACS Catal.*, 2014, **4**, 1171-1181.
54. O. A. Abdelrahman, H. Y. Luo, A. Heyden, Y. Roman-Leshkov and J. Q. Bond, *J. Catal.*, 2015, **329**, 10-21.